Inorganic Chemistry

pubs.acs.org/IC Article

Chemical Bonding Governs Complex Magnetism in $MnPt_5P$

Xin Gui, Ryan A. Klein, Craig M. Brown, and Weiwei Xie*

Cite This: *Inorg. Chem.* 2021, 60, 87−96 Read Online

ACCESS | Metrics & More | Article Recommendations | Supporting Information

ABSTRACT: Subtle changes in chemical bonds may result in dramatic revolutions in magnetic properties in solid-state materials. $MnPt_5P$, a derivative of the rare-earth-free ferromagnetic $MnPt_5As$, was discovered and is presented in this work. $MnPt_5P$ was synthesized, and its crystal structure and chemical composition were characterized by X-ray diffraction as well as energy-dispersive X-ray spectroscopy. Accordingly, $MnPt_5P$ crystallizes in the layered tetragonal structure with the space group *P*4/*mmm* (No. 123), in which the face-shared $Mn@Pt_{12}$ polyhedral layers are separated by P layers. In contrast to the ferromagnetism observed in $MnPt_5As$, the magnetic properties measurements on $MnPt_5P$ show antiferromagnetic ordering occurs at ∼188 K with a strong magnetic anisotropy in and out of the *ab*-plane. Moreover, a spin-flop transition appears when a high magnetic field is applied. An A-type antiferromagnetic structure was obtained from the analysis of powder neutron diffraction (PND) patterns collected at 150 and 9 K. Calculated electronic structures imply that hybridization of Mn-3*d* and Pt-5*d* orbitals is critical for both the structural stability and observed magnetic properties. Semiempirical molecular orbitals calculations on both $MnPt_5P$ and $MnPt_5As$ indicate that the lack of 4*p* character on the P atoms at the highest occupied molecular orbital (HOMO) in $MnPt_5P$ may cause the different magnetic behavior in $MnPt_5P$ compared to $MnPt_5As$. The discovery of $MnPt_5P$, along with our previously reported $MnPt_5As$, parametrizes the end points of a tunable system to study the chemical bonding which tunes the magnetic ordering from ferromagnetism to antiferromagnetism with the strong spin−orbit coupling (SOC) effect.

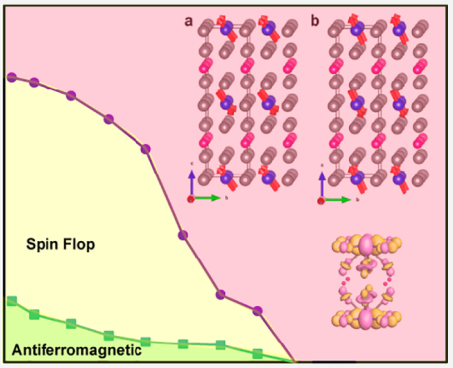

INTRODUCTION

Chemical bonding concepts are critical for understanding and predicting the chemical compositions, structural stabilities, and resulting exotic physical properties in solid-state materials.[1−5] Generally, chemical bonds in solids are directly related to the total energy of formation, which primarily originates from ionic and covalent interactions. Thus, compounds with the same structure show similar energies of formations with distinct chemical bonds due to slight differences in chemical compositions and atomic distances. The subtle changes in chemical bonds become decisive for the physical behaviors, for example, magnetism.[6] Over the past decades, complex intermetallic compounds have been synthesized containing magnetically active Mn atoms with various Mn−Mn configurations, allowing the studies of magnetic exchange as a function of atomic distances and chemical bonding interactions.[7−14] The previous studies revealed a consistent conclusion that magnetic ordering originated from the Mn−Mn interlayer exchange interaction is extremely sensitive to lattice constants of the unit cell and atomic distances due to thermal expansion.[15−18] Moreover, the transformation between ferromagnetic (FM) states and antiferromagnetic (AFM) states can be controlled and manipulated by temperature, pressure, magnetic field (spin-flop), and chemical doping in several systems, such as RMn_6X_6[7−9] and RMn_2X_2 (R = rare-earth elements; X = Sn/Ge).[10−14] Such FM-AFM transitions are suitable for heat assisted magnetic recording (HAMR) technologies.[19−22]

$MnPt_5As$ crystallizes in a layered tetragonal structure with the space group of *P*4/*mmm*, analogous to one of the well-known heavy Fermion superconductors, $CeCoIn_5$.[23,24] $MnPt_5As$ was reported to order ferromagnetically with a large magnetic moment of 3.6 μ_B on Mn at room temperature (T_C ∼ 301 K), indicating a strong Mn−Mn FM exchange interaction.[25] The theoretical assessment on $MnPt_5As$ showed the Mn−Mn antibonding interaction dominates the density of states above and below the Fermi energy allowing the structure to relax through spin polarization. Moreover, the Mn−Mn distance along the *c*-axis is nearly twice as long as the distance in the *ab*-plane, which induces a large anisotropy in and out of the *ab*-plane. A Goodenough-Kanamori style analysis of the structure suggests both intralayer FM superexchange interaction along the 90° Mn−Pt−Mn pathway and a much weaker interlayer FM superexchange interaction along the Mn−Pt−As−Pt−Mn pathway, leading to long-range FM ordering.

Received: August 11, 2020
Published: December 16, 2020

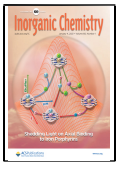

https://dx.doi.org/10.1021/acs.inorgchem.0c02403
Inorg. Chem. 2021, 60, 87−96

To further understand how chemical bonding rules the magnetic, the As ions in $MnPt_5As$ were substituted by the isovalent but much smaller P ions. A new compound, $MnPt_5P$, was designed and synthesized. $MnPt_5P$ crystallizes in the same structure as $MnPt_5As$ and was determined to order antiferromagnetically with $T_N \sim 188$ K. Electronic structure and molecular orbital calculations indicate that the shorter Mn−Mn distance due to the lack of Mn-3d and $P\bar{4}p$ orbital hybridization in $MnPt_5P$ is crucial for the antiferromagnetic interactions. The new antiferromagnetic $MnPt_5P$, along with the previously reported $MnPt_5As$, can be an ideally tunable system to investigate the impact of chemical bonding on magnetic ordering.

EXPERIMENTAL SECTION

Sample Preparation. The procedures for the synthesis of $MnPt_5As$[25] were adapted for the synthesis of polycrystalline $MnPt_5P$. Mn powder, Pt powder, and red P powder were evenly mixed with a molecular ratio of Mn:Pt:P = 1:5:1. The mixture was ground, pressed into a pellet, and then placed into an alumina crucible. The crucible was sealed into an evacuated silica tube ($<10^{-5}$ Torr) and then heated to 1050 °C at a rate of 30 °C per hour. The sample was slowly cooled to room temperature for 2 weeks after annealing at 1050 °C for 2 days. Small single crystals ($\sim 0.8 \times 0.8 \times 0.2$ mm^3) were obtained from the product chunk. Structural characterization and physical properties measurements were performed on the single crystals obtained. $MnPt_5P$ is stable in both air and moisture.

Phase Identification. The powder X-ray diffraction (PXRD) patterns of the synthesized sample were measured with a Rigaku MiniFlex 600 powder X-ray diffractometer equipped with a Cu K_α radiation (λ = 1.5406 Å, Ge monochromator). Data were collected over scattering angle, 2θ, from 5° to 90° with a step of 0.005° at a rate of 0.1°/min. Rietveld analysis was performed using the Fullprof Suite to obtain the weight percentage of obtained phases.[26]

Structure Determination. Single-crystal X-ray diffraction experiments were conducted on a Bruker Apex II diffractometer equipped with Mo radiation ($\lambda_{K\alpha}$ = 0.71073 Å) at room temperature to determine the crystal structure of $MnPt_5P$. Data for multiple crystallites ($\sim 10 \times 60 \times 60$ μm^3) from different batches were collected to ensure homogeneity. Crystals were mounted on a Kapton loop and protected by glycerol. Four distinct combinations of positions for crystals and detector were determined by the software according to the predetermined unit cell. The scanning 2θ width was set to 0.5° with the exposure time of 10 s. The crystal structure was solved based on direct methods and full-matrix least-squares on F^2 models within the *SHELXTL* package.[27] Data acquisition was obtained via Bruker *SMART* software with the corrections on Lorentz and polarization effects done with the *SAINT* program. Numerical absorption corrections due to high concentration of Pt were accomplished with *XPREP*.[28,29]

Powder Neutron Diffraction (PND). The powder sample was loaded into a cylindrical vanadium can and sealed with an indium O-ring inside a He-filled glovebox equipped with oxygen and water sensors. The sample was then mounted on a bottom-loading closed-circuit refrigerator. PND patterns were collected at the National Institute for Standards and Technology Center for Neutron Diffraction high-resolution powder diffractometer BT-1. The data were collected using a Ge(311) monochromator (with in-pile columniation of 60′), which produced a neutron wavelength of λ = 2.0772 Å. Patterns were collected at 295.0(1) K, 150.0(1) K, and 9.0(1) K for 6 h at each temperature.

Scanning Electron Microscope (SEM). Crystal images and chemical compositions were measured and analyzed using a high vacuum scanning electron microscope (SEM) (JSM-6610 LV). Samples were placed on carbon tape prior to loading into the SEM chamber and were examined at 20 kV with an exposure time of 100 s.

Physical Properties Measurements. Physical properties measurements were conducted on a Quantum Design Dynacool Physical Property Measurement System (PPMS) with and without applied fields. Resistivity and magnetic properties were measured from 1.8 to 350 K, while heat capacity data were collected between 1.8 and 225 K. The magnetic susceptibility is defined as $\chi = M/H$ where M is the magnetization in units of emu (10^{-3} Am^2), and H is the applied magnetic field. A standard relaxation calorimetry method was used to measure heat capacity, and the data were collected in a zero magnetic field between 1.8 and 225 K using N-type grease. All the measurements were performed on manually picked single crystal samples of $MnPt_5P$.

Electronic Structure Calculations. The band structure and density of states (DOS) of $MnPt_5P$ were calculated using the WIEN2k program, which has the full-potential linearized augmented plane wave method (FP-LAPW) with local orbitals implemented.[30,31] The electron exchange-correlation potential parametrized by Perdew et al. was used to treat the electron correlation within the generalized gradient approximation.[32] The conjugate gradient algorithm was applied, and the cutoff energy was set at 500 eV. Reciprocal space integrations were completed over a $7 \times 7 \times 4$ Monkhorst−Pack k-points mesh for the nonmagnetic calculation and $8 \times 8 \times 3$ for the magnetic calculation.[33] With these settings, the calculated total energy converged to less than 0.1 meV per atom. The spin−orbit coupling (SOC) effects were only applied for Pt atoms. The structural lattice parameters obtained from SC-XRD are used for both calculations for nonmagnetic calculation, while for magnetic calculation, the magnetic structure obtained from PND was utilized.

Molecular Orbital (MO) Calculation. Semiempirical extended-Hückel-tight-binding (EHTB) methods and CAESAR packages are employed in calculating molecular orbitals of $MnPt_5P$ and $MnPt_5As$.[34] The basis sets for Mn are as follows: s: Hii = −9.7500 eV, $\zeta 1$ = 0.9700, coefficient1 = 1.0000; p: Hii = −5.8900 eV, $\zeta 1$ = 0.9700, coefficient1 = 1.0000; d: Hii = −11.6700 eV, $\zeta 1$ = 5.1500, coefficient1 = 0.5139, $\zeta 2$ = 1.7000, coefficient2 = 0.6929. The basis sets for Pt are as follows: s: Hii = −9.0770 eV, $\zeta 1$ = 2.5540, coefficient1 = 1.0000; p: Hii = −5.4750 eV, $\zeta 1$ = 2.5540, coefficient1 = 1.0000; d: Hii = −12.5900 eV, $\zeta 1$ = 6.0130, coefficient1 = 0.6334, $\zeta 2$ = 2.6960, coefficient2 = 0.5513. The basis sets for P are as follows: s: Hii = −18.60 eV, $\zeta 1$ = 1.750, coefficient1 = 1.0000; p: Hii = −14.00 eV, $\zeta 1$ = 1.300, coefficient1 = 1.0000. The basis sets for As are as follows: s: Hii = −16.2200 eV, $\zeta 1$ = 2.2300, coefficient1 = 1.0000; p: Hii = −12.1600 eV, $\zeta 1$ = 1.8900, coefficient1 = 1.0000.

RESULTS AND DISCUSSION

Crystal Structure and Phase Determination of $MnPt_5P$. The crystal structure of $MnPt_5P$ was determined to be similar to $MnPt_5As$.[25] $MnPt_5P$ crystallizes in a tetragonal

Table 1. Single-Crystal Structure Refinement for $MnPt_5P$ at 300 (2) K

refined formula	$MnPt_5P$
molar density (g/mol)	1061.36
space group; Z	$P4/mmm$; 1
a (Å)	3.8967 (3)
c (Å)	6.9318 (7)
V (Å^3)	105.25 (2)
θ range (deg)	2.939−32.966
extinction coefficient	0.0050 (6)
no. reflections; R_{int}	1378; 0.0386
no. independent reflections	154
no. parameters	11
R_1: ωR_2 ($I > 2\delta(I)$)	0.0197; 0.0410
goodness of fit	1.212
diffraction peak and hole (e$^-$/Å^3)	2.851; −4.362

https://dx.doi.org/10.1021/acs.inorgchem.0c02403
Inorg. Chem. 2021, 60, 87−96

Table 2. Atomic Coordinates and Equivalent Isotropic Displacement Parameters for $MnPt_5P$ at 296(2) K[a]

atom	Wyckoff	occ	x	y	z	U_{eq}
Pt1	1*a*	1	0	0	0	0.0034(2)
Pt2	4*i*	1	0	1/2	0.2915(1)	0.0033(2)
Mn3	1*c*	1	1/2	1/2	0	0.0023(7)
P4	1*b*	1	0	0	1/2	0.005(1)

[a] U_{eq} is defined as one-third of the trace of the orthogonalized U_{ij} tensor (Å^2). Values in parentheses indicate 1 SD.

unit cell with the space group of *P*4/*mmm*. Crystallographic data including refinement results, atomic coordinates, and isotropic displacement parameters are listed in Tables 1 and 2. As shown in Figure 1*a*, the crystal structure of $MnPt_5P$ is analogous to $MnPt_5As$ where the Mn@Pt_{12} polyhedral layers are separated by pnictogen layers (P/As). The character of the layered structural feature can be observed in the SEM image in Figure S1. Both Mn and P atoms adopt into one equivalent site, respectively, while two atomic sites are occupied by Pt atoms, marked as Pt1 and Pt2. The Mn−Pt distance within the *ab*-plane is 2.751 (1) Å in $MnPt_5P$ and 2.780 (1) Å in $MnPt_5As$, and the Mn−Pt−Mn angle is constrained by symmetry to be 90° in both materials. Meanwhile, the Mn−Pt distance along the *c*-axis is 2.803 (1) Å in $MnPt_5P$ and 2.791 (1) Å in $MnPt_5As$. Moreover, the binary phase $MnPt_3$ consists of similar Mn@Pt_{12} polyhedra with identical Mn−Pt distances of 2.758(1) Å and Mn−Pt−Mn bond angles of 90°. Interestingly, the shortest Mn−Mn distances for $MnPt_5P$, $MnPt_5As$, and $MnPt_3$ are 3.891(1) Å, 3.931(1) Å, and 3.900(1) Å, respectively. Meanwhile, the Mn−Mn interatomic distances are 6.921(3) Å and 7.092(2) Å in $MnPt_5P$ and $MnPt_5As$ between Mn layers. $MnPt_5As$ and $MnPt_3$ were reported to be ferromagnetically ordered with $T_c \sim 301$ and 390 K, respectively. However, $MnPt_5P$ shows no ferromagnetic ordering at room temperature but an antiferromagnetic ordering at $T_N \sim 188$ K. Details will be discussed in the following paragraphs.

Powder X-ray diffraction (PXRD) was carried out on the polycrystalline $MnPt_5P$. The PXRD pattern and Rietveld fits are illustrated in Figure 1*b*. Two additional phases, $MnPt_3$ and Pt, were included in the refinement as impurities resulting in no unindexed reflections. The goodness-of-fit parameters, R_p, R_{wp}, and χ^2, were determined to be 8.03%, 11.0%, and 2.39, respectively, which indicates a reasonable pattern fitting. The weight percentage of two magnetic phases, $MnPt_5P$ and $MnPt_3$, appeared to be 97(1) wt % and 1.01(2) wt %.

Magnetic Properties of $MnPt_5P$ Crystals. The magnetic properties of $MnPt_5P$ were measured on select single crystals. The single crystals were prealigned using the single crystal X-ray diffractometer before loading. The measurements were performed on the same crystallites with two distinct orientations. One is perpendicular to the *c*-axis of the crystal (B⊥*c*), as shown in Figure 2*a*, *c*, and *e*; and the other one is parallel to the *c*-axis (B//*c*), shown in Figure 2*b*, *d*, and *f*.

The temperature-dependence of magnetic susceptibility along two different directions as well as their inversed susceptibility is illustrated in Figure 2*a* and *b*. The measurements were conducted under an applied magnetic field of 1000 Oe ((1000/4π) A/m) from 1.8 to 350 K. A large difference in susceptibility values could be easily found along two directions (the susceptibility ~5 emu/Oe/mol (1 emu/Oe/mol = 4π 10^{-6} m^3/mol) for B⊥*c* but ~1.2 emu/Oe/mol for B//*c* at 1.8 K). This indicates strong magnetic anisotropy. Meanwhile, a

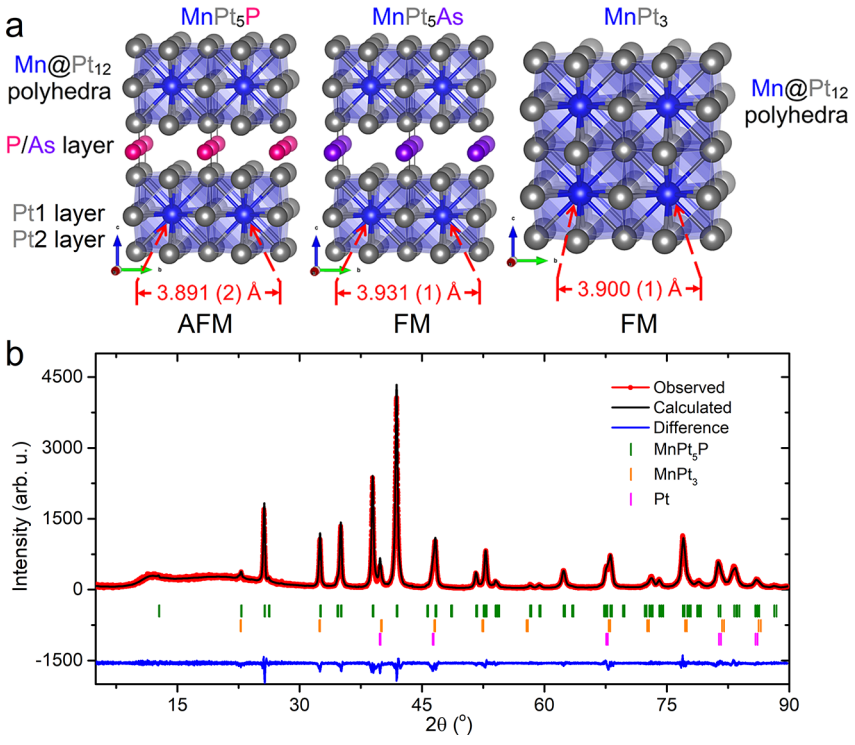

Figure 1. *a*. Crystal structures of $MnPt_5P$, $MnPt_5As$, and $MnPt_3$ where blue, gray, red, and purple spheres represent Mn, Pt, P, and As atoms, respectively (AFM: antiferromagnetic; FM: ferromagnetic.) *b*. Powder XRD pattern of $MnPt_5P$ refined by the Rietveld method. The red line with a circle, black line, and blue line are the observed, calculated patterns, and residual intensities, respectively. Green, orange, and pink vertical ticks indicate the Bragg peaks' positions for $MnPt_5P$, $MnPt_3$, and Pt, respectively.

https://dx.doi.org/10.1021/acs.inorgchem.0c02403
Inorg. Chem. 2021, 60, 87−96

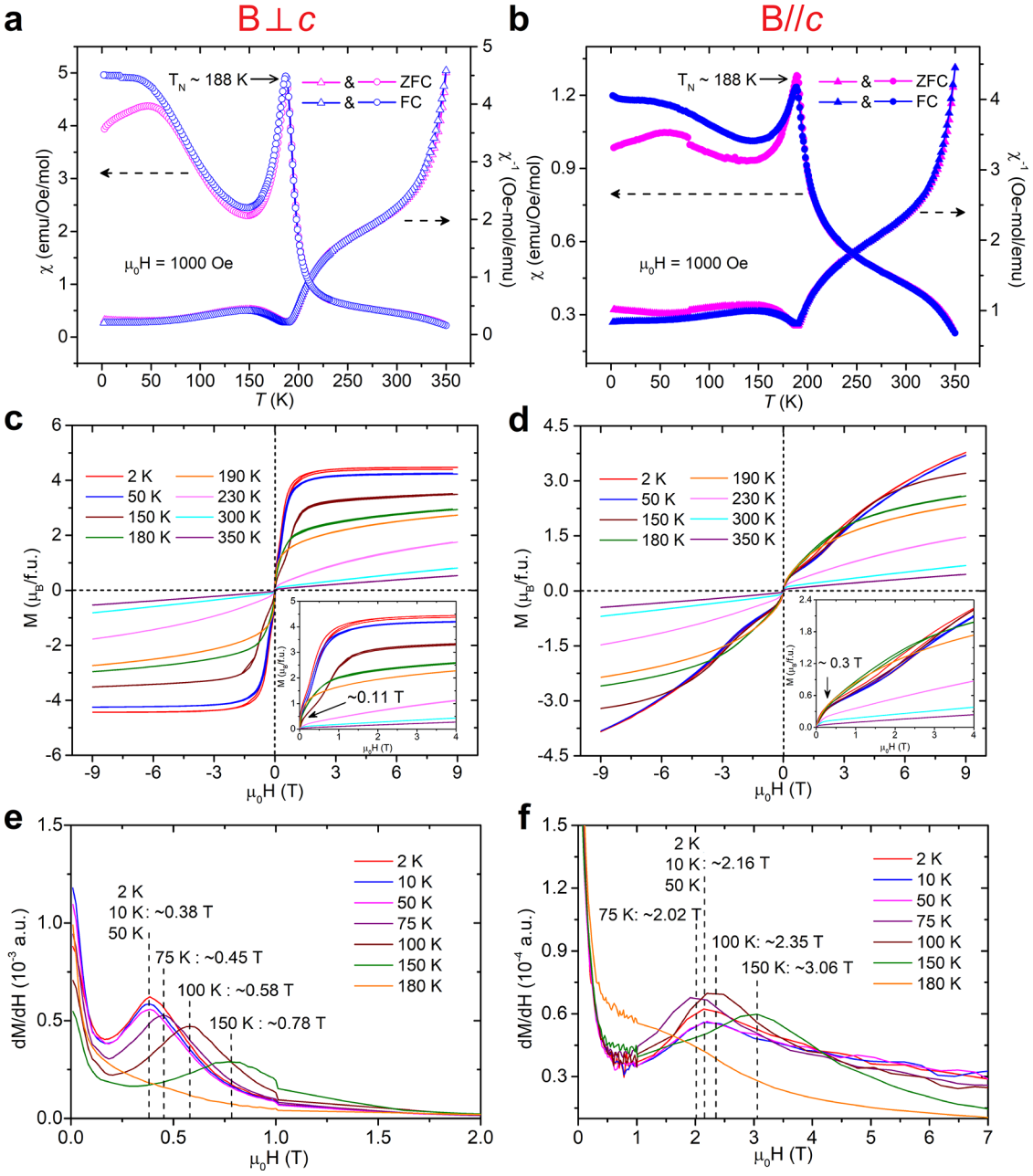

Figure 2. Temperature-dependence of magnetic susceptibility for $MnPt_5P$ under an applied magnetic field of 1000 Oe when the field is *a*. perpendicular to the *c*-axis (B⊥*c*) and *b*. parallel to the *c*-axis (B//*c*). Field-dependence of magnetization for $MnPt_5P$ under various temperatures when the field is *c*. perpendicular to the *c*-axis (B⊥*c*) and *d*. parallel to the *c*-axis (B//*c*). *e*. and *f*. present d*M*/d*H* vs the applied field indicating the spin-flop field. One Oe = $(1000/4\pi)$ A/m.

sharp antiferromagnetic ordering transition peak could be observed in both sweep directions at a Néel temperature (T_N) ~ 188 K. Below the transition temperature, the magnetic susceptibility started dropping with decreasing temperature and reached the minimum at ~147 K. Below ~147 K, the magnetic susceptibility increased and achieved a plateau below 50 K under the Field-Cooling (FC) measurement. In the Zero-Field-Cooling (ZFC) mode, the magnetic susceptibility showed similar trends, except that the magnetic susceptibility decreased below 50 K. Above the Néel temperature, the inverse susceptibility did not show a linear behavior due to the slight ferromagnetic $MnPt_3$ impurity which orders at ~390 K.

Figure 2*c* and *d* present the hysteresis loops of $MnPt_5P$ under various temperatures. A small coercive field (<200 Oe) was detected, an indication of soft magnetic behaviors in $MnPt_5P$. Figure 2*c* showed a ferromagnetic-like loop. A clear magnetic anisotropy could be seen based on the distinct saturated field for two field orientations. At 2 K, the saturated moment for B⊥*c* is ~4.49 μ_B/f.u., while no saturation was achieved for the other direction. This indicates that in $MnPt_5P$, the easy axis lies within the *ab*-plane. Meanwhile, a metamagnetic phase transition can be seen by referring to the upturn of magnetization with an increasing magnetic field at low-field regions for both directions below T_N, as shown in the insets of Figure 2*c* and *d*. In Figure 2*e* and *f*, d*M*/d*H* with respect to the applied magnetic field showed peaks for this metamagnetic phase transition, which could be a spin-flop transition. During the transition, the spin-flop field, H_{SF},

https://dx.doi.org/10.1021/acs.inorgchem.0c02403
Inorg. Chem. 2021, 60, 87−96

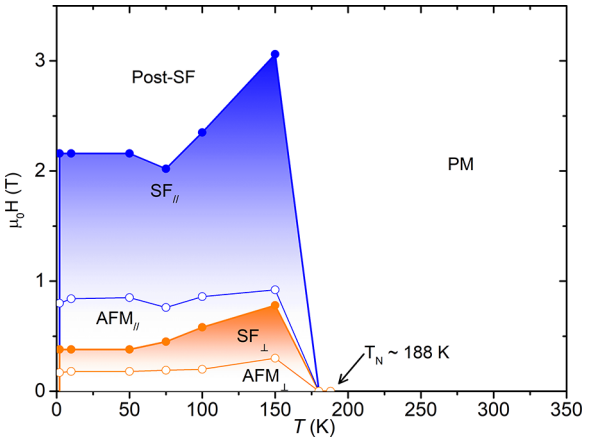

Figure 3. Magnetic phase diagram of $MnPt_5P$. PM: paramagnetic state; AFM: antiferromagnetic state; SF: spin-flop. The open and solid circles were extracted from Figure 2*e* and *f* which represent the beginning and the end of spin-flop transition, respectively. //: the external magnetic field is applied parallelly to the *c* axis; ⊥: the external magnetic field is applied perpendicularly to the *c* axis.

moved toward higher fields with increasing temperature. The value of H_{SF} also exhibited strong magnetic anisotropy referring to the large difference between H_{SF}'s for the two directions. Figure 3 presents the magnetic phase diagram of $MnPt_5P$. The data were extracted from Figure 2*e* and *f*. Above $T_N \sim 188$ K, $MnPt_5P$ is paramagnetic, while below ~150 K, a spin-flop transition emerged in both crystallographic orientations. Notably, after the spin-flop transition (as shown by the post-SF region in Figure 3), $MnPt_5P$ shows ferromagnetic ordering with a saturated moment when B⊥*c* as discussed previously. However, $MnPt_5P$ did not exhibit saturated magnetization below 9 T when B//*c*. A kink can be found for both $SF_{//}$ and $AFM_{//}$. It can be speculated that the spin

Table 3. Irreducible Representations (IR) and Corresponding Basis Vectors (BV) for the Magnetic Mn Ion at the (1/2, 1/2, 0) Fractional Coordinates and Associated Real Magnetic Components in the *a*-, *b*-, and *c*-Axis Directions for the $\vec{k} = (00^1/_2)$ Propagation Vector in the *P4/mmm* Space Group

		basis vector components		
IR	BV	$m_{\|a}$	$m_{\|b}$	$m_{\|c}$
Γ_3	ψ_1	0	0	16
Γ_9	ψ_2	8	0	0
Γ_9	ψ_3	0	−8	0

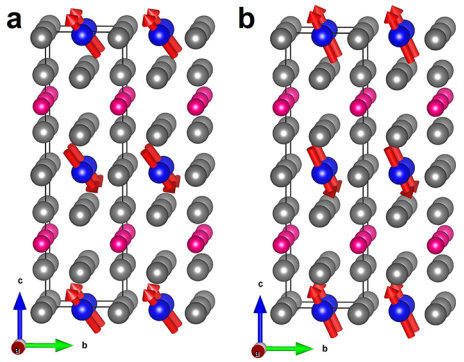

Figure 5. Magnetic structures of $MnPt_5P$ at *a*. 9 K and *b*. 150 K.

reorientation can happen between 100 and 50 K so that it makes the spin-flop transition happen at a lower magnetic field due to the lower energy required.

Magnetic Structures of $MnPt_5P$. To determine the magnetic structure of $MnPt_5P$, the powder neutron diffraction patterns at 295, 150, and 9 K were analyzed using the Topas Academic,[35] EXPGUI/GSAS,[36,37] and FullProf suite[38] soft-

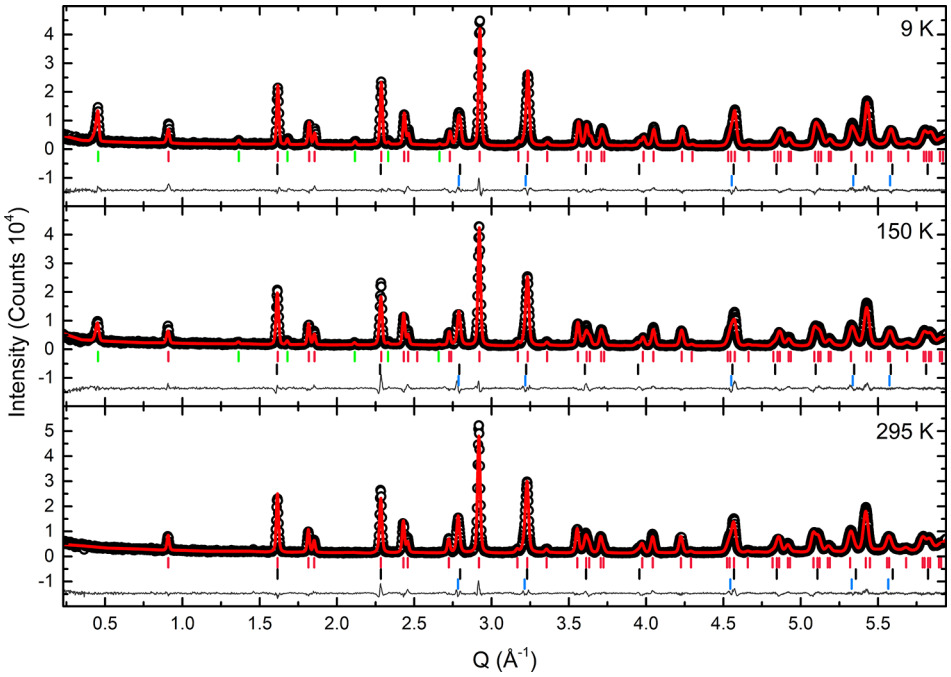

Figure 4. Fitted powder neutron diffraction patterns of $MnPt_5P$ at *a*. 9 K, *b*. 150 K, and *c*. 295 K. The black circle, red line, and gray line stand for the observed pattern, calculated pattern, and residual intensities. Red, blue, and black vertical ticks represent the Bragg peak positions for $MnPt_5P$, Pt, and $MnPt_3$. Green vertical tick marks denote the magnetic Bragg peak positions for $MnPt_5P$.

https://dx.doi.org/10.1021/acs.inorgchem.0c02403
Inorg. Chem. 2021, 60, 87−96

Table 4. Projection on Each Crystal Axis from Magnetic Moments on Mn in $MnPt_5P$[a]

translation	crystal axis	moments at 9 K/μ_B	moments at 150 K/μ_B
(0, 0, 0)	*a*	1.997(1)	1.394(1)
	b	−2.129(1)	−1.740(1)
	c	0.887(1)	1.108(1)
(0, 0, 1)	*a*	−1.997(1)	−1.394(1)
	b	2.129(1)	1.740(1)
	c	−0.887(1)	−1.108(1)
total moment		3.051	2.490

[a]Values in parentheses indicate 1 SD.

ware packages. An initial Pawley fit of the pattern collected at 295 K again revealed Pt and $MnPt_3$ as minority impurity phases.[39,40] A subsequent thorough Rietveld refinement of the $MnPt_5P$ phase yielded the nuclear crystal structure at 295 K.[41] During this analysis, the total scattering arising from the ferromagnetic $MnPt_3$ impurity was treated as a single phase using a Pawley phase, while the Pt phase was treated using a full Rietveld refinement.

At 150 K, six additional Bragg peaks appeared in the diffraction pattern. Given that Pt is diamagnetic, $MnPt_3$ is ferromagnetic, and that the antiferromagnetic ordering temperature for $MnPt_5P$ is $T_N \approx 188$ K, the new Bragg peaks were assigned as magnetic Bragg peaks arising from long-range antiferromagnetic ordering in $MnPt_5P$. The new Bragg peaks were indexed to a doubling of the unit cell in the *c*-axis direction for the $MnPt_5P$ phase. At 150 K, the resulting Miller indices for the six new Bragg peaks are (001), (003), (101), (103), (111), and (113) at $Q \approx 0.46$ Å^{-1}, 1.37 Å^{-1}, 1.68 Å^{-1}, 2.12 Å^{-1}, 2.33 Å^{-1}, and 2.65 Å^{-1}, respectively (Figure 4). Each pattern is plotted individually (Figures S2−S4), and an enhanced view of the magnetic Bragg peaks in the 9 K pattern with the corresponding refinement curve, which illustrates the quality of the refinement, is shown in the Supporting Information (Figure S5).

The *k*-search functionality in FullProf confirmed a commensurate magnetic propagation vector of $\vec{k} = (00^1/_2)$. Representational analysis of the $\vec{k} = (00^1/_2)$propagation vector in the parent *P4/mmm* space group using SARA*h*[33] in conjunction with the FullProf suite led to three unique irreducible representations with basis vectors, which are summarized in Table 3.

Each irreproducible representation accounts for magnetic scattering in a single unit cell direction in real space. Given the nonzero intensity of the (111) magnetic Bragg peak, all three irreducible representations were required to accurately model the antiferromagnetic phase for $MnPt_5P$ at 150 K. The basis vector mixing coefficients were refined freely during the Rietveld refinement fitting for the 150 K pattern. The same analysis was conducted for the neutron powder diffraction pattern collected at 9 K. At 9 K, the pattern shows an increase in intensity of the six magnetic Bragg peaks arising from $MnPt_5P$, corresponding to an increase in the magnitude of the magnetic moments. The analysis of the nuclear and magnetic phases resulted in the magnetic structure for $MnPt_5P$ at 150 and 9 K as shown in Figure 5. These two magnetic structures agree qualitatively. At both temperatures, the material is a canted A-type antiferromagnetic with the spins nearly aligned along the (110) crystallographic plane in real space, with canting in the *c*-axis direction. The resulting magnetic moments for the Mn ions are summarized in Table 4.

The A-type antiferromagnetism in $MnPt_5P$ is distinct from the ferromagnetism exhibited by the isostructural $MnPt_5As$ and the structurally similar $MnPt_3$ compounds. The magnetic measurements show that, by chemical substitution with P, the interlayer Mn−Mn FM interaction is replaced by an interlayer AFM exchange coupling interaction. A simple Goodenough-Kanamori type analysis of the $MnPt_5P$ crystal structure suggests that the magnitude of the interlayer FM super-exchange interaction should be enhanced in $MnPt_5P$ compared to $MnPt_5As$, because the bond angles along the Mn−Pt−Pnictogen−Pt−Mn pathway remain relatively constant while the bond lengths decrease significantly with P substitution assuming that the nature of the Pt-Pnictogen bonding remains constant. Therefore, we hypothesized that a change in the nature of the Pt−Pnictogen bonding effectively drives the magnitude of the interlayer FM superexchange interaction to zero, and a through-space AFM interaction becomes the dominant interlayer magnetic exchange interaction. To test this hypothesis, we performed DFT calculations to investigate the nature of the metal−pnictogen bonding near the Fermi surface.

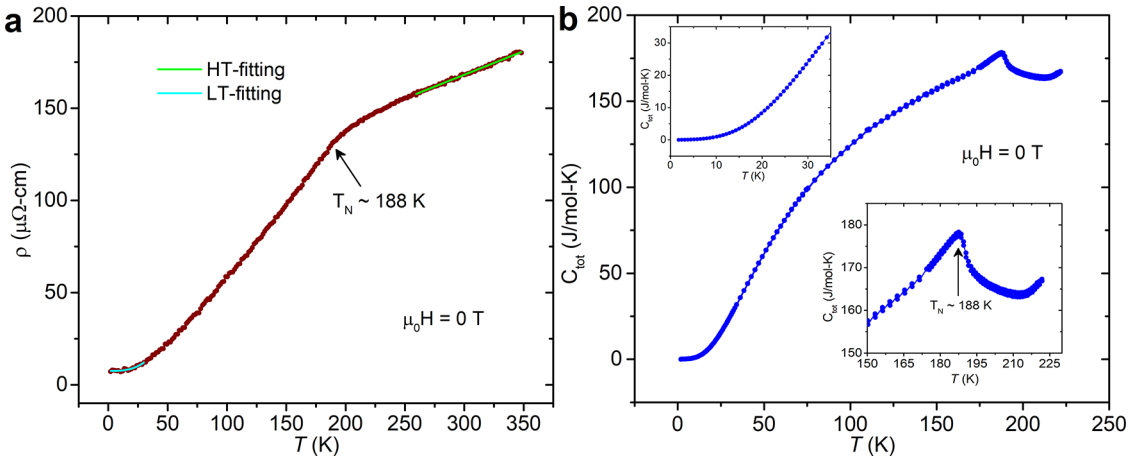

Figure 6. *a*. Temperature-dependence of resistivity of $MnPt_5P$ between 2 and 350 K. Green and cyan lines represent the fitting lines for high-temperature (HT) and low-temperature (LT) regions. *b*. Heat capacity curve of $MnPt_5P$ from 1.8 to 225 K.

https://dx.doi.org/10.1021/acs.inorgchem.0c02403
Inorg. Chem. 2021, 60, 87−96

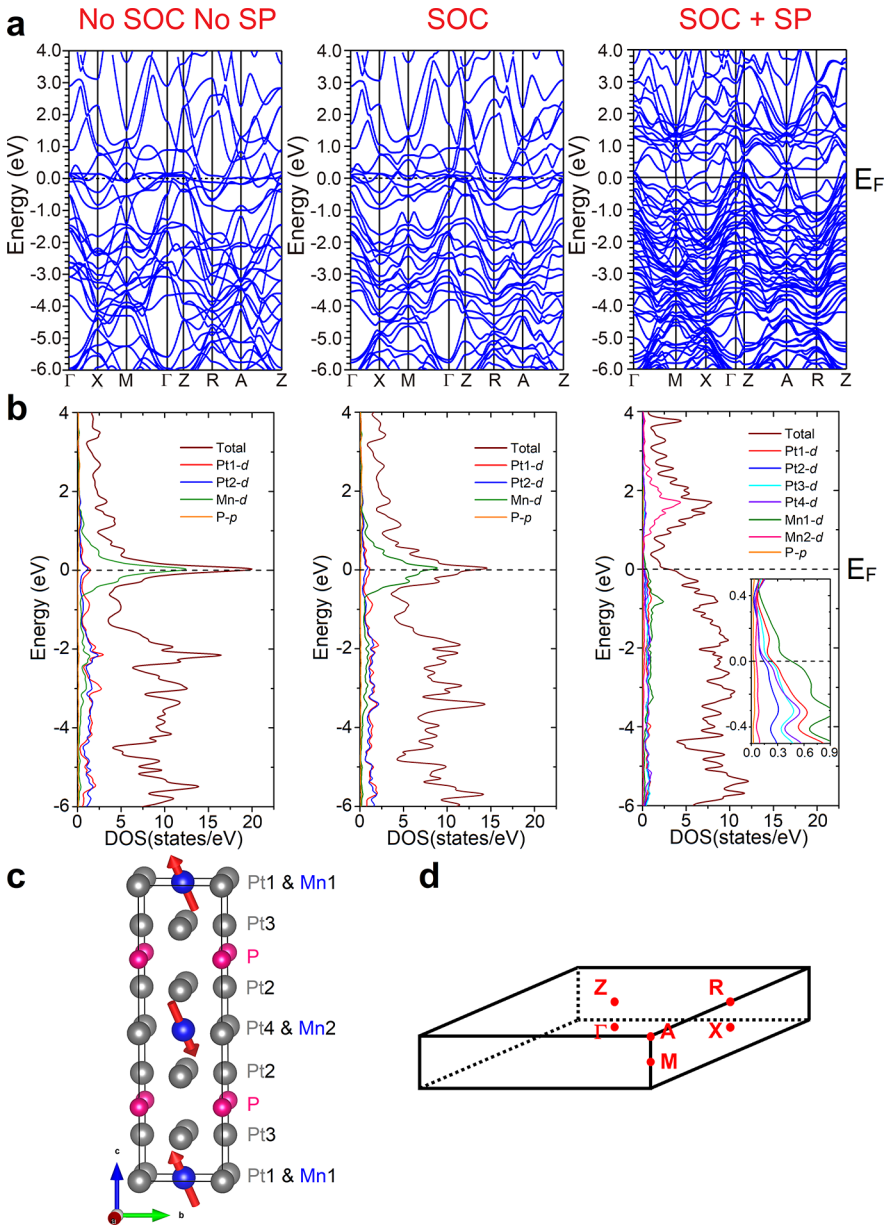

Figure 7. *a*. Band structures calculated for $MnPt_5P$ with/without consideration of the SOC effect and SP. *b*. Density of states corresponding to *a*. *c*. Magnetic structure of $MnPt_5P$ at 9 K with atomic sites labeled. *d*. Brillouin zone utilized for calculation with SP.

Resistivity and Heat Capacity Measurements. Resistivity measurement was carried out between 2 and 350 K without an applied magnetic field on the single crystal measured for magnetic properties. The four-probe method was employed to make the electrical contacts with the Ag point. The temperature-dependence of resistivity shown in Figure 6*a* demonstrates metallic behavior with the small resistivity. The high RRR value ($\rho_{300K}/\rho_{2K} \sim 23.6$) indicates the high quality and lack of defects in the crystal. A sudden drop in resistivity could be found around $T_N \sim 188$ K, which is consistent with the antiferromagnetic ordering transition of $MnPt_5P$. T^1 and T^3 behaviors were fitted for high-temperature (260 K−350 K) and low-temperature (2 K−30 K) regions, respectively, by using the following equation: $\rho(T) = \rho_0 + AT^n$ where ρ_0 is the residual resistivity due to defect scattering, A is a constant, and n is an integer determined by the interaction pattern. The results implied that above T_N, the resistivity of $MnPt_5P$ was mainly generated by electron−phonon collision, while at low temperature, the *s*-*d* electron scattering took over.

Heat capacity measurements were conducted between 1.8 and 225 K without an applied magnetic field on the same crystal measured for resistivity and magnetism. As can be seen in Figure 6*b*, with decreasing temperature, an abrupt and large upturn could be found below 195 K, and the maximum was reached at ∼188 K, where antiferromagnetic ordering occurs. Other than that, no more phase transition peaks could be found in the lower temperature region. Due to the lack of determination of the phonon mode contributions, the magnetic entropy change could not be calculated. Magnetism, resistivity, and heat capacity results are in good agreement with each other.

Electronic Structures and Molecular Orbital Diagram. The electronic structure of $MnPt_5P$ was calculated including spin−orbit coupling (SOC) effects and spin-polarization (SP). The electronic structure calculation with SP was performed

https://dx.doi.org/10.1021/acs.inorgchem.0c02403
Inorg. Chem. 2021, 60, 87−96

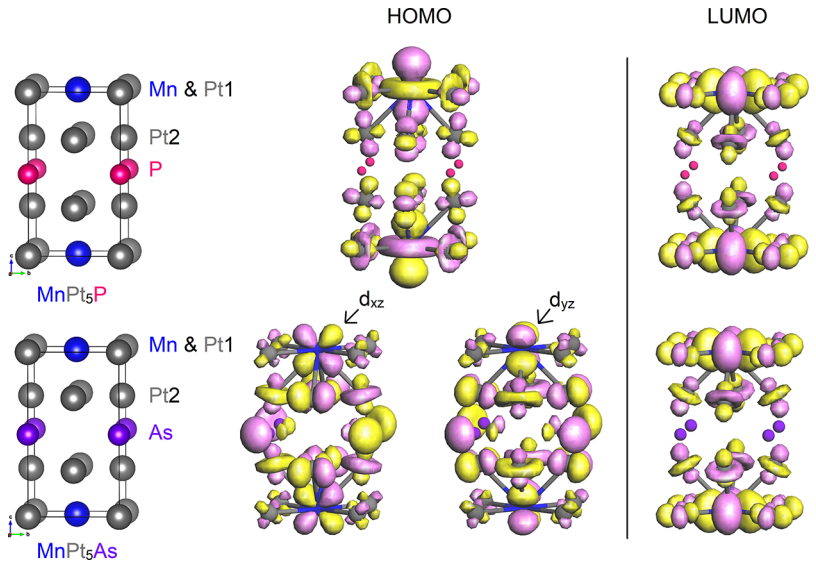

Figure 8. Highest occupied molecular orbitals (HOMOs) and lowest unoccupied molecular orbitals (LUMOs) of $MnPt_5P$ and $MnPt_5As$.

with the magnetic unit cell shown in Figure 7*c* labeled with atomic sites, i.e., with a doubled unit cell of the crystal structure, and the Brillouin Zone (BZ) appeared in Figure 7*d*.

Figure 7*a* displays the band structure of $MnPt_5P$ from −6.0 to 4 eV, while the enlarged figure showing from −1.0 to 1.0 eV is shown as in the SI as Figure S6. The dense bands observed around the Fermi level indicate the metallic properties of $MnPt_5P$, which is consistent with the resistivity measurements. One can see that with consideration of the SOC effect, the bands near the Fermi level (E_F) split, i.e., at the Γ point. By taking SP into account, the bands were found to be denser below and above E_F due to a doubling of the unit cell. However, the bands near E_F were fewer and more dispersive, that is, fewer "flat bands". The projection from crucial orbitals of atoms on distinct atomic sites was listed in Figure S7. This analysis revealed that Mn-*d* and Pt-*d* orbitals were dominant near E_F. However, the most significant contribution to the DOS from the P atoms came from the P-*p* orbital, but this was not as critical as Mn-*d* and Pt-*d* orbitals near E_F. With inclusion of the SOC effect, the band intensity was dramatically decreased. While SOC and SP were both considered, the Mn1 site dominates near E_F with the Mn2 site more effective above the Fermi level. In Figures S8 and S9, we show the projection of each *d* orbital of Mn and Pt and the *p* orbital of the P atom with consideration of SOC and SP. The d_z^2 orbital of both Mn sites is dominant above and below E_F which is consistent with the results calculated by extended-Hückel-tight-binding (EHTB) methods shown in the next section. For Pt2 and Pt3 sites, E_F crosses the d_{xy} orbital, while other orbitals ($d_{x^2-y^2}$, d_{xz}, d_{yz}, and d_z^2) contribute less to bands near E_F. For the Pt1 site, each *d* orbital, especially d_{xy} and d_{xz} + d_{yz}, contributes the most, while similar results can be found for the Pt2 site, which are distinct with EHTB results. One of the possible reasons might be that in DFT calculation, we calculated the band structure for the AFM sublattice, while in EHTB, a normal crystal lattice was taken into account. The density of states (DOS) corresponding to the calculated band structures are presented in Figure 7*b*. The DOS at E_F is reduced when SOC was considered and dropped dramatically when both SOC and SP were included in the calculations. In Figure 7*b* (right), a pseudogap appears at ∼0.4 eV above E_F, and a van Hove singularity emerges at ∼−0.3 eV. The van Hove singularity is alleviated when SP effects are included in the calculation. Thus, future doping work may be appropriate to be performed to achieve higher density of states at E_F to obtain interesting physical properties due to the possible strong electron correlation, such as spin−lattice coupled superconductivity. Moreover, as can be seen in the inset of Figure 7*b* (right), the contribution from Mn1 and all Pt sites was dominant at the Fermi level. The low density of states comparing with other calculations without consideration of SP is due to the antiferromagnetic ordering of Mn atoms.

Chemical Bonding in $MnPt_5P$ and $MnPt_5As$. To estimate the chemical bond influence on atomic interactions and magnetic behavior in $MnPt_5P$ and $MnPt_5As$, molecular orbital diagrams were generated based on the semiempirical extended-Hückel-tight-binding (EHTB) methods using the CAESAR packages,[42] shown in Figure 8. All the molecular orbitals exhibited antibonding features in both $MnPt_5P$ and $MnPt_5As$. The lowest unoccupied molecular orbitals (LUMOs) for both compounds appeared the same where Mn, Pt1, and Pt2 atoms show $d_{x^2-y^2}$, $d_{x^2-y^2}$, and d_z^2 character. No contribution could be found from the pnictogen atomic sites. However, significant differences are observed when it came to the highest occupied molecular orbitals (HOMOs). $MnPt_5P$ was found to adopt one HOMO where d_z^2 orbitals of Mn and Pt1 were dominant, while Pt2 presented d_{xz} character; and no contribution was found for the P atom. On the other hand, in $MnPt_5As$, two degenerate HOMOs appeared (Figure 8) and showed similar components. Mn and Pt1 in the HOMOs of $MnPt_5As$ are dominated by d_{xz} and d_{yz} orbitals, while $d_{x^2-y^2}$ and d_z^2 were important at the Pt2 site. Interestingly, even though the P atoms in $MnPt_5P$ did not show any major contribution in the HOMO, the As atoms in $MnPt_5As$ showed strong *p* character. Thus, we speculate that the lack of available *p* character in P may result in a shorter bond distance, reduce possible orbital overlap, and differentiate magnetic superexchange mechanisms from $MnPt_5As$. This allows an AFM interlayer through space magnetic coupling, presumably present in both pnictogen congeners, to dominate the interlayer magnetic exchange interaction in $MnPt_5P$.

https://dx.doi.org/10.1021/acs.inorgchem.0c02403
Inorg. Chem. 2021, 60, 87−96

CONCLUSION

A novel antiferromagnet, $MnPt_5P$, was designed and synthesized a using high-temperature solid-state reaction. $MnPt_5P$ contains a layered 2D crystal structure and displays magnetic anisotropy. A spin-flop transition was detected when high magnetic fields were applied. The magnetic structure was determined to be an A-type antiferromagnetic by powder neutron diffraction experiments. The theoretical calculations showed the crucial significance of *d* electrons from Mn and Pt atoms on structural stability and magnetic behaviors. The comparison on molecular orbital calculation results between $MnPt_5P$ and the previously reported ferromagnetic $MnPt_5As$ revealed that the lack of P-*p* character in the $MnPt_5P$ HOMO may explain the antiferromagnetic ordering. $MnPt_5P$ and reported $MnPt_5As$ provide an ideal platform to tune ferromagnetic and antiferromagnetic ordering in the family compounds with the same structure and valence electron counts either by chemical doping or by the application of extreme pressures. As shown in Figure S10, the EV curve generated from $MnPt_5As$ indicates that doping P onto the As site is energy favored and might be able to tune ferromagnetic and antiferromagnetic ordering in this system.

ASSOCIATED CONTENT

Supporting Information

The Supporting Information is available free of charge at https://pubs.acs.org/doi/10.1021/acs.inorgchem.0c02403.

SEM image of $MnPt_5P$ crystal; powder neutron diffraction patterns with Rietveld refinement fit curve; projections from critical orbitals of different atoms on band structure, EV curve of $MnPt_5As$, anisotropic thermal displacements from $MnPt_5P$, and atomic coordinates and isotropic thermal parameters for $MnPt_5P$ (PDF)

Accession Codes

CCDC 2039428 contains the supplementary crystallographic data for this paper. These data can be obtained free of charge via www.ccdc.cam.ac.uk/data_request/cif, or by emailing data_request@ccdc.cam.ac.uk, or by contacting The Cambridge Crystallographic Data Centre, 12 Union Road, Cambridge CB2 1EZ, UK; fax: +44 1223 336033.

AUTHOR INFORMATION

Corresponding Author

Weiwei Xie − *Department of Chemistry and Chemical Biology, Rutgers University, Rutgers, New Jersey 08854, United States;* orcid.org/0000-0002-5500-8195; Email: weiwei.xie@rutgers.edu

Authors

Xin Gui − *Department of Chemistry, Princeton University, Princeton, New Jersey 08540, United States;* orcid.org/0000-0003-0616-2150

Ryan A. Klein − *Chemistry and Nanoscience Department, National Renewable Energy Laboratory, Golden, Colorado 80401, United States; NIST Center for Neutron Research, National Institute of Standards and Technology, Gaithersburg, Maryland 20899, United States*

Craig M. Brown − *NIST Center for Neutron Research, National Institute of Standards and Technology, Gaithersburg, Maryland 20899, United States*

Complete contact information is available at: https://pubs.acs.org/10.1021/acs.inorgchem.0c02403

Notes

Certain commercial equipment, instruments, or materials are identified in this document. Such identification does not imply recommendation or endorsement by the National Institute of Standards and Technology, nor does it imply that the products identified are necessarily the best available for the purpose. The views and opinions of the authors expressed herein do not necessarily state or reflect those of the United States Government or any agency thereof. Neither the United States Government nor any agency thereof, nor any of their employees, makes any warranty, expressed or implied, or assumes any legal liability or responsibility for the accuracy, completeness, or usefulness of any information, apparatus, product, or process disclosed, or represents that its use would not infringe privately owned rights.

The authors declare no competing financial interest.

ACKNOWLEDGMENTS

The work is supported by a Beckman Young Investigator award and NSF-DMR-2053287. R.A.K. acknowledges funding by the U.S. Department of Energy (USDOE), Office of Energy Efficiency and Renewable Energy (EERE), Fuel Cell Technologies Office (FCTO) under contract no. DE-AC36-8GO28308 to the National Renewable Energy Laboratory (NREL).

REFERENCES

(1) Zhang, J.; Song, L.; Sist, M.; Tolborg, K.; Iversen, B. B. Chemical bonding origin of the unexpected isotropic physical properties in thermoelectric Mg_3Sb_2 and related materials. *Nat. Commun.* **2018**, *9*, 4716.

(2) Miller, G. J.; Zhang, Y.; Wagner, F. R. Chemical bonding in solids. *Handbook of Solid State Chemistry* **2017**, 405−489.

(3) Grin, Y. Inhomogeneity and anisotropy of chemical bonding and thermoelectric properties of materials. *J. Solid State Chem.* **2019**, *274*, 329−336.

(4) Cagnoni, M.; Führen, D.; Wuttig, M. Thermoelectric Performance of IV−VI Compounds with Octahedral-Like Coordination: A Chemical-Bonding Perspective. *Adv. Mater.* **2018**, *30*, 1801787.

(5) Zhong, G. H.; Wang, X. H.; Wang, R. S.; Han, J. X.; Zhang, C.; Chen, X. J.; Lin, H. Q. Structural and bonding characteristics of potassium-doped p-terphenyl superconductors. *J. Phys. Chem. C* **2018**, *122*, 3801−3808.

(6) Sifkovits, M.; Smolinski, H.; Hellwig, S.; Weber, W. Interplay of chemical bonding and magnetism in Fe_4N, Fe_3N and ζ-Fe_2N. *J. Magn. Magn. Mater.* **1999**, *204*, 191−198.

(7) Zhang, S. Y.; Zhao, P.; Cheng, Z. H.; Li, R. W.; Sun, J. R.; Zhang, H. W.; Shen, B. G. Magnetism and giant magnetoresistance of $YMn_6Sn_{6-x}Ga_x$ (x = 0−1.8) compounds. *Phys. Rev. B: Condens. Matter Mater. Phys.* **2001**, *64*, 212404.

(8) Venturini, G.; El Idrissi, B. C.; Malaman, B. Magnetic properties of RMn_6Sn_6 (R= Sc, Y, Gd−Tm, Lu) compounds with $HfFe_6Ge_6$ type structure. *J. Magn. Magn. Mater.* **1991**, *94*, 35−42.

(9) Venturini, G.; Welter, R.; Malaman, B. Crystallographic data and magnetic properties of RT_6Ge_6 compounds (R≡Sc, Y, Nd, Sm, Gd-Lu; T≡Mn, Fe). *J. Alloys Compd.* **1992**, *185*, 99−107.

(10) Narasimhan, K. S. V. L.; Rao, V. U. S.; Bergner, R. L.; Wallace, W. E. Magnetic properties of RMn_2Ge_2 compounds (R= La, Ce, Pr, Nd, Cd, Tb, Dy, Ho, Er, and Th). *J. Appl. Phys.* **1975**, *46*, 4957−4960.

(11) Szytuła, A.; Szott, I. Magnetic properties of ternary RMn_2Si_2 and RMn_2Ge_2 compounds. *Solid State Commun.* **1981**, *40*, 199−202.

(12) Van Dover, R. B.; Gyorgy, E. M.; Cava, R. J.; Krajewski, J. J.; Felder, R. J.; Peck, W. F. Magnetoresistance of $SmMn_2Ge_2$: A layered

antiferromagnet. *Phys. Rev. B: Condens. Matter Mater. Phys.* **1993**, *47*, 6134.
(13) Brabers, J. H. V. J.; Bakker, K.; Nakotte, H.; De Boer, F. R.; Lenczowski, S. K. J.; Buschow, K. H. J. Giant magnetoresistance in polycrystalline $SmMn_2Ge_2$. *J. Alloys Compd.* **1993**, *199*, L1−L3.
(14) Brabers, J. H. V. J.; Nolten, A. J.; Kayzel, F.; Lenczowski, S. H. J.; Buschow, K. H. J.; De Boer, F. R. Strong Mn-Mn distance dependence of the Mn interlayer coupling in $SmMn_2Ge_2$-related compounds and its role in magnetic phase transitions. *Phys. Rev. B: Condens. Matter Mater. Phys.* **1994**, *50*, 16410.
(15) Bai, V. S.; Rajasekharan, T. Evidence of a critical Mn-Mn distance for the onset of ferromagnetism in NiAs type compounds. *J. Magn. Magn. Mater.* **1984**, *42*, 198−200.
(16) Wang, Q.; Sun, Q.; Jena, P.; Kawazoe, Y. Antiferromagnetic Coupling Driven by Bond Length Contraction near the $Ga_{1-x}Mn_xN$ Film Surface. *Phys. Rev. Lett.* **2004**, *93*, 155501.
(17) Li, S.; Ao, Z.; Zhu, J.; Ren, J.; Yi, J.; Wang, G.; Liu, W. Strain controlled ferromagnetic-antiferromagnetic transformation in Mn-doped silicene for information transformation devices. *J. Phys. Chem. Lett.* **2017**, *8*, 1484−1488.
(18) Brabers, J. H. V. J.; Buschow, K. H. J.; De Boer, F. R. Field-induced first-order antiferromagnetic-ferromagnetic transitions in RMn_2Ge_2 compounds and their relation to the magnetostriction of the Mn sublattice. *Phys. Rev. B: Condens. Matter Mater. Phys.* **1999**, *59*, 9314.
(19) Shiroishi, Y.; Fukuda, K.; Tagawa, I.; Iwasaki, H.; Takenoiri, S.; Tanaka, H.; Mutoh, H.; Yoshikawa, N. Future options for HDD storage. *IEEE Trans. Magn.* **2009**, *45*, 3816−3822.
(20) Thiele, J. U.; Maat, S.; Fullerton, E. E. FeRh/FePt exchange spring films for thermally assisted magnetic recording media. *Appl. Phys. Lett.* **2003**, *82*, 2859−2861.
(21) Thiele, J. U.; Maat, S.; Robertson, J. L.; Fullerton, E. E. Magnetic and structural properties of FePt-FeRh exchange spring films for thermally assisted magnetic recording media. *IEEE Trans. Magn.* **2004**, *40*, 2537−2542.
(22) Sasakawa, T.; Tagawa, N. Reduction of magnetic field in vehicle of superconducting maglev train. *IEEE Trans. Magn.* **2000**, *36*, 3676−3679.
(23) Movshovich, R.; Jaime, M.; Thompson, J. D.; Petrovic, C.; Fisk, Z.; Pagliuso, P. G.; Sarrao, J. L. Unconventional Superconductivity in $CeIrIn_5$ and $CeCoIn_5$: Specific Heat and Thermal Conductivity Studies. *Phys. Rev. Lett.* **2001**, *86*, 5152.
(24) Petrovic, C.; Pagliuso, P. G.; Hundley, M. F.; Movshovich, R.; Sarrao, J. L.; Thompson, J. D.; Fisk, Z.; Monthoux, P. Heavy-Fermion Superconductivity in $CeCoIn_5$ at 2.3 K. *J. Phys.: Condens. Matter* **2001**, *13*, No. L337.
(25) Gui, X.; Xie, W. Crystal Structure, Magnetism, and Electronic Properties of a Rare-Earth-Free Ferromagnet: $MnPt_5As$. *Chem. Mater.* **2020**, *32*, 3922−3929.
(26) Rodríguez-Carvajal, J. Recent advances in magnetic structure determination by neutron powder diffraction. *Phys. B* **1993**, *192*, 55−69.
(27) Sheldrick, G. M. Crystal Structure Refinement with SHELXL. *Acta Crystallogr., Sect. C: Struct. Chem.* **2015**, *71*, 3−8.
(28) Bruker. *Smart*; Bruker AXS, Inc.: Madison, WI, USA, 2012. https://www.bruker.com/products/x-ray-diffraction-and-elemental-analysis/single-crystal-x-ray-diffraction/sc-xrd-software/overview/sc-xrd-software/apex3.html (accessed 2020-04-10).
(29) Walker, N.; Stuart, D. An Empirical Method for Correcting Diffractometer Data for Absorption Effects. *Acta Crystallogr., Sect. A: Found. Crystallogr.* **1983**, *39*, 158−166.
(30) Blaha, P.; Schwarz, K.; Sorantin, P.; Trickey, S. B. Full-Potential, Linearized Augmented Plane Wave Programs for Crystalline Systems. *Comput. Phys. Commun.* **1990**, *59*, 399−415.
(31) Wimmer, E.; Krakauer, H.; Weinert, M.; Freeman, A. J. Full-Potential Self-Consistent Linearized-Augmented-Plane-Wave Method for Calculating the Electronic Structure of Molecules and Surfaces: O_2 Molecule. *Phys. Rev. B: Condens. Matter Mater. Phys.* **1981**, *24*, 864−875.
(32) Perdew, J. P.; Wang, Y. Accurate and Simple Analytic Representation of the Electron-Gas Correlation Energy. *Phys. Rev. B: Condens. Matter Mater. Phys.* **1992**, *45*, 13244−13249.
(33) King-Smith, R. D.; Vanderbilt, D. Theory of Polarization of Crystalline Solids. *Phys. Rev. B: Condens. Matter Mater. Phys.* **1993**, *47*, 1651−1654.
(34) Hoffmann, R. An extended Hückel theory. I. hydrocarbons. *J. Chem. Phys.* **1963**, *39*, 1397−1412.
(35) Coelho, A. *Topas Academic v6*; Coelho Software: 2017. http://www.topas-academic.net/ (accessed 2020-12-12).
(36) Larson, A. C.; Von Dreele, R. B. *General Structure Analysis System (GSAS)*; Los Alamos National Laboratory Report LAUR 86-748; 2000.
(37) Toby, B. H. EXPGUI, a graphical user interface for GSAS. *J. Appl. Crystallogr.* **2001**, *34*, 210−213.
(38) Buschow, K. V.; Van Engen, P. G.; Jongebreur, R. Magneto-optical properties of metallic ferromagnetic materials. *J. Magn. Magn. Mater.* **1983**, *38*, 1−22.
(39) Pawley, G. S. Unit-cell refinement from powder diffraction scans. *J. Appl. Crystallogr.* **1981**, *14*, 357−361.
(40) Rietveld, H. M. A profile refinement method for nuclear and magnetic structures. *J. Appl. Crystallogr.* **1969**, *2*, 65−71.
(41) Wills, A. S. A new protocol for the determination of magnetic structures using simulated annealing and representational analysis (SARAh). *Phys. B* **2000**, *276*, 680−681.
(42) Ren, J.; Liang, W.; Whangbo, M. H. *CAESAR 2.0 package for Windows*; 2002.

https://dx.doi.org/10.1021/acs.inorgchem.0c02403
Inorg. Chem. 2021, 60, 87−96